

Learning Object Compliance via Young’s Modulus from Single Grasps using Camera-Based Tactile Sensors

Michael Burgess, Jialiang Zhao

Department of Mechanical Engineering

Massachusetts Institute of Technology (MIT), United States

mburgjr@mit.edu

Abstract:

Compliance is a useful parametrization of tactile information that humans often utilize in manipulation tasks. It can be used to inform low-level contact-rich actions or characterize objects at a high-level. In robotic manipulation, existing approaches to estimate compliance have struggled to generalize across object shape and material. Using camera-based tactile sensors, proprioception, and force measurements, we present a novel approach to estimate object compliance as Young’s modulus E from parallel grasps. We evaluate our method over a novel dataset of 285 common objects, which includes a wide array of shapes and materials with Young’s moduli ranging from 5.0 kPa to 250 GPa. Data is collected over automated parallel grasps of each object. Combining analytical and data-driven approaches, we develop a hybrid system using a multi-tower neural network to analyze a sequence of tactile images from grasping. This system is shown to estimate the Young’s modulus of unseen objects within an order of magnitude at 74.2% accuracy across our dataset. This is a drastic improvement over purely analytical and data-driven baselines which exhibit 28.9% and 65.0% accuracy respectively. Importantly, this estimation system performs irrespective of object geometry and demonstrates robustness across object materials. Thus, it could be applied in a general robotic manipulation setting to characterize unknown objects and inform decision-making, for instance to sort produce by ripeness.

Keywords: Robotic Manipulation, Tactile Sensing, Compliance

1 Introduction

General and robust object compliance estimation could significantly enhance robotic perception systems. For instance, a ripe avocado appears visually identical to an unripe avocado, yet their compliance differs greatly. Without the ability to accurately estimate compliance, a robot cannot effectively distinguish between such visually similar objects. Compliance measurement has proven valuable in multiple applications, including identifying the ripeness of fruits and vegetables [1, 2, 3, 4] and in biomedical fields [5, 6, 7]. In the future, a universal compliance estimation architecture could be applied in assembly or recycling processes to inform decisions based on object material.

In robotics, we seek to replicate the human ability to perceive properties like compliance through touch [8]. Humans naturally use tactile information to characterize objects and inform interactions [9]. In the case of compliance, we sense discrepancies between soft and hard objects through fingertip pressure and deformation [10]. High-resolution, camera-based tactile sensors like GelSight are specifically designed to track the deformation of a robotic fingertip during contact [11, 12].

However, even with the help of high-resolution tactile sensing, achieving human-like compliance perception remains challenging, especially in unstructured environments. An object’s deformation in response to loading depends on both its shape and material composition. Thus, without known geometry and pose tracking, analytical methods cannot be utilized to rigorously determine compli-

ance [13]. Alternatively, learning-based implementations have been developed to estimate compliance from tactile images alone without the use of mechanical modeling [14, 5, 15, 1]. While these methods have demonstrated relative success in estimating compliance independent of shape, they still face limitations in describing compliance across a wide range of materials.

We aim to create a compliance estimation system that is robust to both shape and material by integrating analytical modeling with machine learning. Young’s modulus (E) is a fundamental property in mechanical modeling that offers a measure of compliance for nearly all materials [16]. By parameterizing compliance using Young’s modulus, we can seamlessly incorporate analytical models and create estimates of compliance on a universal scale. Our hybrid approach leverages the strengths of analytical modeling to better generalize across materials, while using learning techniques to address complexities posed by diverse geometries. Specifically, we use a neural network to fuse CNN-encoded tactile images with estimates from analytical contact models. We train our approach across a novel dataset of 285 common objects, including a wide variety of shapes and materials.

Our primary contribution is a novel compliance estimation architecture which demonstrates increased accuracy over the current state-of-the-art. Additionally, we contribute a novel dataset which could be used in the development of future compliance estimation architectures. Using our diverse dataset, we validate that our hybrid estimation approach can generalize well across object shape and material. Thus, our estimation system could be applied in general robotic manipulation to characterize unknown objects and inform decision-making. This is especially beneficial in scenarios where visually similar objects may have distinct material composition.

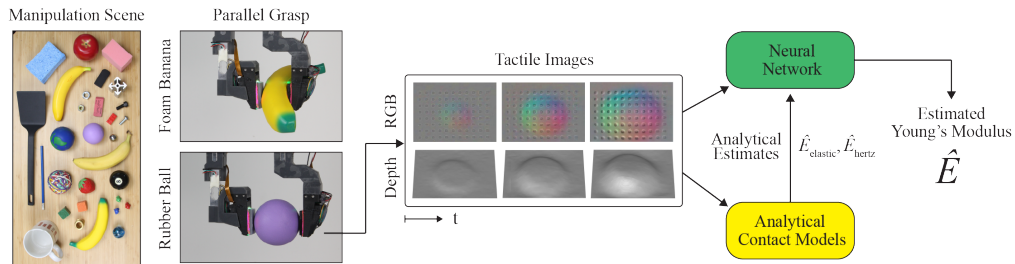


Figure 1: **Young’s modulus estimation system.** Tactile images from parallel grasps of various objects are fed into learned models alongside analytical estimates to generate a hybrid estimate of Young’s modulus. Tactile images are size 35mm by 25mm.

2 Related Work

2.1 GelSight Sensors & Contact Modeling

Camera-based tactile sensors, such as GelSight sensors, are designed to track contact geometry in high-resolution using a camera placed behind an elastomer gel pad [12, 17, 18, 19, 20, 21]. They are highly effective for sensing texture [22, 23, 24], contact force [12], friction [25], and object shape and pose [26, 27]. However, reliably modeling contact with these soft sensors remains challenging. Simulators have been developed to generate tactile images and deformed geometry of sensors using pre-computed finite element method (FEM) solutions [28]. Finite element analysis has proven a viable way to model soft contact on hardware and used to estimate forces from tactile data [29, 30]. Though modeling with FEM is accurate, it requires a precise map of object geometry and solutions often must be pre-computed offline.

Alternative approaches have been developed using Hertzian mechanics to model soft contact in robotic grasping [31, 32]. This closed-form method offers improved computational efficiency over FEM and simulated methods. Still, it requires assumptions on contact geometry, namely that geometry should be axisymmetric. Hertzian contact models have been utilized for force estimation [33, 5] and surface curvature detection from tactile data [34]. These closed-form constitutive models can easily be inverted to determine object compliance.

2.2 Compliance Estimation

Estimating the compliance of a contacted object remains a complex problem in robotic manipulation, particularly without assumptions on object shape or material type. Analytical approaches to compliance estimation often lack robustness to variations in geometry. A traditional approach to model compliance is to apply Hooke’s Law using measurements of grasping force and positions [13]. Similar models have been foundational in developing low-level grasping control policies [35, 36]. This method can provide an effective stiffness of grasping, but may struggle when applied to unknown objects with complex shapes. By incorporating tactile sensing, it is possible to create higher fidelity compliance estimation models [37, 38, 39]. These methods have a stronger ability to sense and generalize across contact geometry but still struggle to account for complex contact geometries.

Recent learning-based approaches to compliance estimation have demonstrated the ability to better generalize across geometry but struggle when applied over a wide-range of material types. Data-driven architectures have been developed to estimate the Shore 00 hardness of an object in contact with a GelSight sensor directly from tactile images without any mechanical modeling [40, 14]. The Shore 00 hardness scale is designed to quantify the compliance of soft rubbers [41]. This model is trained using exclusively rubber objects and is thus fundamentally limited to this material domain. Alternatively, LLM-backed methods have been developed to classify tactile images with binary semantic descriptions of ‘soft’ or ‘hard’ [15, 1]. These large data models are promising but have not been used to assess finer differences in compliance on a continuous scale. Other data-driven implementations have been developed using tactile sensing to directly measure the ripeness of produce [2, 3, 4]. As before, these methods are restricted by their dataset and labeling method. In all cases, labeling choices inhibit models from integrating analytical modeling alongside learning.

3 Methods

3.1 Overview

We develop a hybrid system that fuses analytical models alongside learning to estimate the Young’s modulus of general unknown objects from a single parallel grasp. Through analytical modeling, we can create a well-founded, preliminary estimate for Young’s modulus. By incorporating learning, we can compensate for assumptions taken by analytical models to better generalize across contact geometry. A large, diverse dataset of 285 common objects is collected to train and evaluate our method. Our approach of combining analytical models with data-driven methods is partially inspired by residual physics architectures [42] and physics-informed tactile models [43].

Our hybrid estimation architecture is displayed in Fig. 2. After grasping, tactile images and measurements of force F and gripper width w are fed into analytical models to fit respective estimates of Young’s modulus \hat{E}_{elastic} , \hat{E}_{hertz} . In parallel, a selected number N_{frames} of tactile images from a single sensor are processed through a CNN. Features extracted from these images are concatenated with grasp measurements F, w into a large fully-connected decoder. This multi-tower network is similar to other grasp-based architectures [44]. Output features from the large decoder are sent to a smaller decoder alongside analytical estimates to produce a final hybrid estimate of Young’s modulus \hat{E} .

Code for the project is publicly available on [GitHub](#). Collected data for multiple grasps of all objects with labeled Young’s moduli and Shore hardness is publicly available on [HuggingFace](#).

3.2 Analytical Contact Models

Simple Elasticity: Parallel grasping can be modeled as uniaxial loading using an adaptation of Hooke’s Law. A diagram of parallel grasping is provided in Fig. 3. At every instance t , force F is applied to the grasped object, with gripper at width w . Traditional methods have used these measurements alone to estimate the compliance or stiffness of grasped objects [13].

With camera-based tactile sensors, we can increase the fidelity of the model by measuring contact area A and depth d [12]. Contact area A is determined by masking depth images with constant

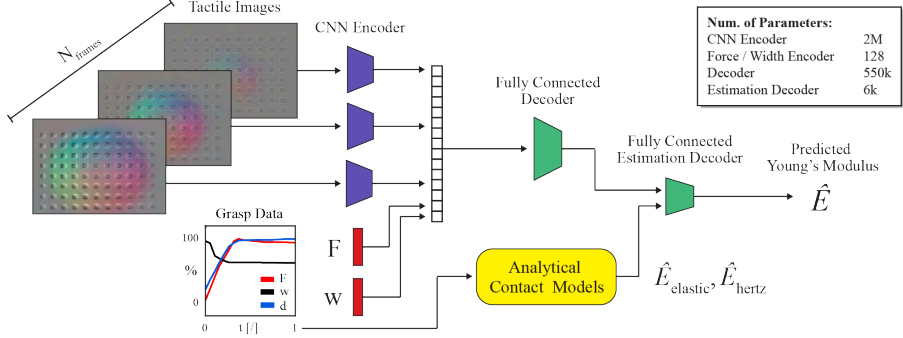


Figure 2: **Young’s modulus estimation architecture.** Tactile images, depth, and measured grasping force F and width w are sent into analytical and learned models. Estimates from analytical models are fed into a fully-connected decoder alongside learned grasp features.

threshold of 0.1mm. This threshold was chosen empirically to cancel out potential noise. Without tactile sensing, we could not measure depth ($d(t) = 0$) and would need to assume constant contact area ($A(t) = A_{\text{sensor}}$). We calculate contact stress σ and object strain ϵ , following Eq. 1. This model assumes symmetry between parallel fingers. We define $t = 0$ to be the moment of first contact, where $F(t = 0)$ must be greater than an empirically-defined threshold.

$$\sigma(t) = \frac{F(t)}{A(t)}, \quad \epsilon(t) = \frac{\Delta w(t) + 2\Delta d(t)}{w(0) + 2d(0)} = \frac{(w(t) + 2d(t)) - (w(0) + 2d(0))}{w(0) + 2d(0)} \quad (1)$$

In the elastic regime, stress σ and ϵ are related by Young’s modulus [16]. Using measurements across grasping time t , we fit an estimate for Young’s modulus \hat{E}_{elastic} following Eq. 2.

$$\sigma = \hat{E}_{\text{elastic}} \epsilon \quad (2)$$

Despite its simplicity, this method does not properly consider object geometry and implicitly assumes a consistent profile along the grasping axis. Furthermore, it overlooks precise information about the deformation of contact geometry that is apparent through high-resolution tactile data.

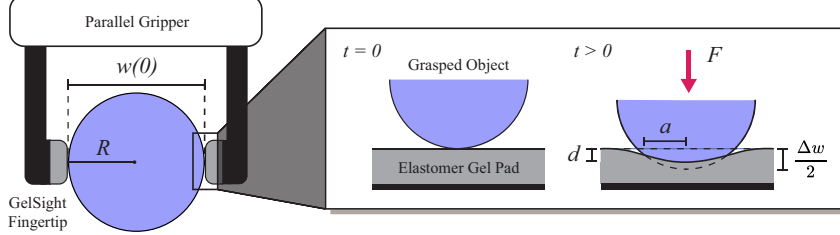


Figure 3: **Simple mechanics of parallel grasping.** Spherical object of radius R is grasped with soft GelSight sensors. Normal force F is applied at width w . Penetration depth d and contact radius a can be measured with tactile sensors. Timestep $t = 0$ is the moment of first contact over the grasp.

Hertzian Contact: Hertzian contact theory models the deformation of elastic bodies in contact [45]. In a simple case, contact is assumed to be without friction or adhesion [46, 47]. Unlike the previous method, Hertzian mechanics closely analyzes geometry through contact. It has been applied to model soft contact in robotics [18, 5], including for GelSight-like tactile sensors [31, 34, 18, 5].

GelSight sensors are made with highly elastic silicone rubber [17]. Unless a grasped object is fully rigid, we expect both bodies to deform through contact. This implies the maximum measured penetration depth d will be less than the relative displacement between the finger and object $d < \frac{\Delta w}{2}$. This phenomenon is depicted in Fig. 3. An aggregate modulus E^* describes the bodies’ combined resistance to deformation in Eq. 3, which depends on the Poisson’s ratio ν of each body.

$$E^* = \left(\frac{1 - \nu_{\text{sensor}}^2}{E_{\text{sensor}}} + \frac{1 - \nu_{\text{obj}}^2}{E_{\text{obj}}} \right)^{-1} \quad (3)$$

Hertzian solutions have been derived for a wide range of contact geometries [48]. We model the sensor as a flat plane. Although we are analyzing contact with an object whose shape is unknown, we model the geometry of all grasped objects as spherical. This simplification is reasonable for convex objects, but may produce bounded errors over our geometrically diverse dataset. Our neural network can learn to compensate for this intrinsic and repeatable geometric modeling error.

Since we assume contact profiles are spherical, we calculate contact radius a based on observed total contact area A . Additionally, we calculate the apparent radius of the unknown object R using contact area and gripper displacement [48]. Using these parameters, we can relate depth d to normal force F via the method of dimensionality reduction (MDR) [48, 49], as formulated in Eq. 4. More detailed derivation for the MDR is provided in Appendix A. With these equations established and measurements over the duration of a grasp, we apply least-squares to retrieve a best fit value \hat{E}^* .

$$a(t) = \sqrt{\frac{A(t)}{\pi}}, \quad R(t) = \frac{a^2(t)}{\Delta w(t)}, \quad d = \frac{1 - \nu_{\text{sensor}}^2}{E_{\text{sensor}}} \left(\frac{3\hat{E}^{*2}F}{32R^2} \right)^{\frac{1}{3}} a \quad (4)$$

We compute an estimated modulus for our unknown object \hat{E}_{hertz} through Eq. 5, given known properties of our sensor $E_{\text{sensor}} = 0.275 \text{ MPa}$, $\nu_{\text{sensor}} = 0.48$. We assume constant $\nu_{\text{obj}} = 0.4$ based on the Poisson's ratio of common materials [50]. After analytical estimates are computed, linear scaling is added to account for potential constant errors across the dataset.

$$\hat{E}_{\text{hertz}} = (1 - \nu_{\text{obj}}^2) \left(\frac{1}{\hat{E}^*} - \frac{1 - \nu_{\text{sensor}}^2}{E_{\text{sensor}}} \right)^{-1} \quad (5)$$

4 Physical Dataset

A novel physical dataset of 285 objects was gathered to train and validate our method. For comparison, our dataset is nearly 4 times larger than the YCB dataset, which includes only 77 objects [51]. Chosen objects were intended to be among things a robotic manipulator may commonly interact with in general operation. Additionally, each object was required to have approximately uniform material composition to ensure that an accurate Young's modulus could be defined for the object and used to label data for supervised training. A subset of dataset objects is displayed in Fig. 4.

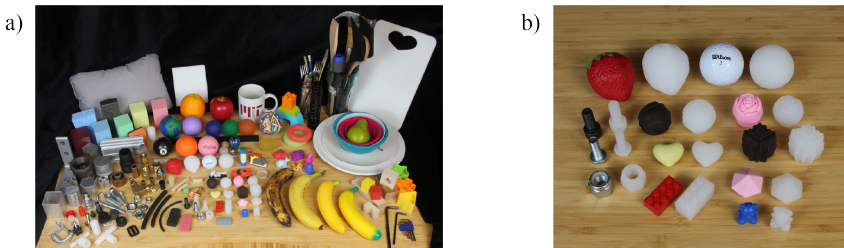


Figure 4: **Physical dataset.** (a) Selected objects from our physical dataset are displayed. These are common objects with a wide variety of shapes and materials. (b) Some custom objects are molded out of silicone to replicate the shape of non-rubber objects in the dataset.

To evaluate how well estimation algorithms could generalize, diversity of shape and material was prioritized in acquiring objects. Thus, we mold 20 custom objects out of silicone to replicate the exact shape of other objects in the dataset with vastly different material composition. Molded objects are displayed in Fig. 4b. Training on data collected across object replicas of different materials will help prevent overfitting to shapes and textures. Moreover, there is incentive to bias towards rubber objects because it is clear from Eq. 5 that it will be easiest to discriminate between Young's moduli nearest to our sensor's. The dataset's composition is further detailed in Appendix E.

As objects were gathered, they were labeled with their Young's moduli. For harder objects, like those made of plastics and metals, this was done by referencing an engineering database of known material properties [52]. For softer objects, like those made of rubber, Shore hardness was measured and

converted to Young’s modulus using Gent’s model of hardness and other established methods [41, 53]. These models provide a reliable measure of object compliance on a logarithmic scale. The dataset includes materials ranging from foam to steel, with Young’s moduli from 5.0 kPa to 250 GPa. For reference, our sensor’s Young’s modulus is 0.275 MPa.

5 Experiments

5.1 Hardware Setup

GelSight Wedge sensors [17] were rigidly attached to a standard parallel robotic gripper with 3D-printed plastic fingers, as depicted in Fig. 5. Although we choose GelSight sensors for our experiment, other flat, camera-based tactile sensors capable of tracking depth in high-resolution would be suitable. One sensor is inscribed with markers. As explained in Appendix B, markers help enhance the dynamic information in a tactile image by tracking surface displacement. Data from only one sensor is required for estimation, but we collect data with both sensors simultaneously to later assess the necessity of markers in estimating Young’s modulus. Additionally, we assume symmetry between fingers in our analytical models. Normal force is measured through a gauge embedded in the left finger. Gripper position is directly measured from control software.

5.2 Data Collection & Training

Data Collection: Automated parallel grasps are executed on objects in fixed position. For each object in our dataset, a set number of grasps are recorded. Objects are re-oriented between each grasp to diversify potential antipodal grasp locations. During grasping, tactile images from GelSight sensors, forces, and gripper widths, are recorded at 30 Hz. Measurements are synchronized by shifting for latency between cameras. Grasps are executed at constant velocity up to force of 30 N. Raw data collected from grasps of spherical objects is plotted in Fig. 6. More details about processing data collected from grasps is provided in Appendix C.

Tactile and depth images at grasping force of 30 N for a set of example objects are depicted in Fig. 7. We observe that textures are more finely captured for rigid object’s with higher modulus. As expected by Eq. 4, peak depth is higher for objects of the same shape with higher modulus.

Data Preprocessing: Data recorded from grasping objects is clipped to include only the loading sequence from first contact to peak force. Misaligned grasps where loading is non-monotonic are disregarded. From here, a set number of frames $N_{\text{frames}} = 3$ are sampled equidistantly in time. Multiple augmentations of samples are taken from each grasp. As depicted in Fig. 2, tactile images are sent as inputs to our multi-tower architecture alongside analytical estimates and force and width measurements. Images are randomly transformed with horizontal and vertical flipping.

Training: We train our model for 80 iterations over 4,000 grasp inputs. In total, these grasps include more than 12,000 tactile images. Output labels are normalized on a log10 scale given the range of Young’s moduli in our dataset. Final sigmoid activation function is used with an MSE loss function.

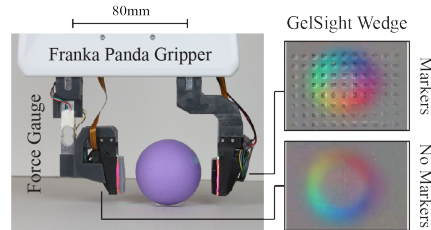


Figure 5: **Hardware setup for data collection.** GelSight Wedge sensors are attached to Franka Panda gripper with embedded force gauge. Normal force is measured through a gauge embedded in the left finger. Gripper position is directly measured from control software.

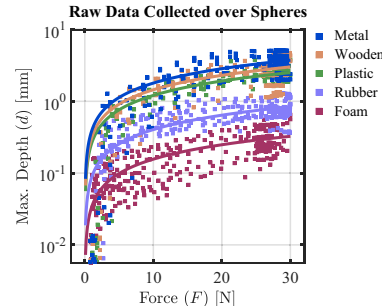


Figure 6: **Raw force and depth data.** Data is collected across grasps for spheres of each material type and fit to $d \sim F^{\frac{2}{3}}$, per our Hertzian model.

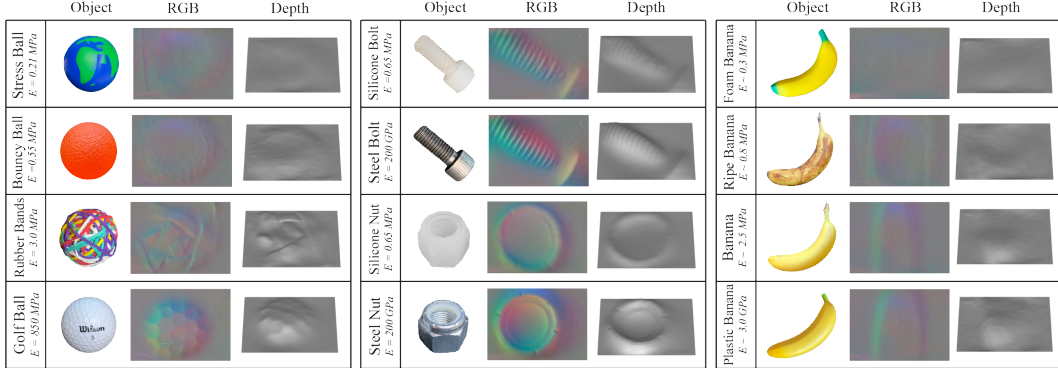


Figure 7: **Example tactile data.** Tactile images and depth reconstruction from a GelSight Wedge sensor without markers over a set of example objects. Shown frames are all from peak pressing force of 30 N. Tactile images are size 35mm by 25mm.

6 Experimental Results

Initially, we train an instance of our model using only rubber objects from our dataset. From Eq. 5, we expect it will be easier to discern fine differences in compliance between rubber objects, as their Young’s modulus is closest to that of our sensor. Estimations across unseen objects for this model are plotted in Fig. 8. The model demonstrates 100% prediction accuracy within an order of magnitude of ground truth Young’s modulus, with an average log10 error of 0.36. We utilize this reduced training configuration to compare our architecture against previously developed Shore hardness models [14]. As detailed in Appendix D, our hybrid system exhibits reduced error over this limited domain.

Subsequently, we train our neural network over the entire collected dataset and compare against analytical baselines. Predictions across unseen objects for each method are plotted in Fig. 9. A traditional Hooke’s Law method without tactile sensing fails to distinguish between material types. Simple elastic and Hertzian analytical models exhibit stronger performance, but remain less than 30% accurate. Our hybrid learned model showcases dramatic improvements over all methods.

In Table 1, performance is compared between different estimation methods and inputs. Performance metrics are computed for grasps of both seen and unseen objects. We evaluate models on a logarithmic scale given the range of Young’s moduli in our dataset. We compute error as the average difference between prediction and ground truth on a log10 scale. Predictions are considered accurate within the same order of magnitude of ground truth labels. This tolerance is deemed sufficient for downstream tasks of produce sorting based on the change in compliance of selected fruits and vegetables during ripening [54, 55, 56, 57].

From the ablation study, we observe that our hybrid model drastically out-performs purely analytical and learning-based methods. RGB tactile images with markers are shown to be most favorable for this estimation task. There is not significant difference in results between models which consider force F and width w measurements. This may be due to the fact that all objects were grasped with identical peak force. Moreover, force is implicitly apparent through tactile difference images [12]. Importantly, analytical estimates \hat{E}_{elastic} , \hat{E}_{hertz} are shown to improve prediction accuracy by nearly 10%. This indicates that a hybrid approach to compliance estimation is favorable over purely learning-based methods, which have been previously explored [14, 15, 1, 2, 3, 4]. Prediction

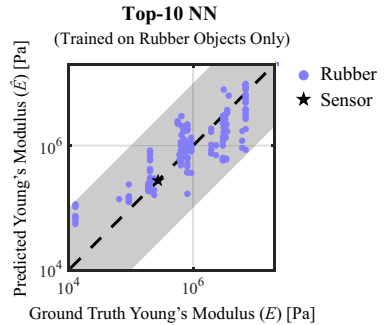


Figure 8: **Young’s modulus predictions for rubber objects only.** Results for model trained on only rubber objects over 80 randomly sampled grasps of unseen objects. Predictions in the gray region are considered sufficiently accurate.

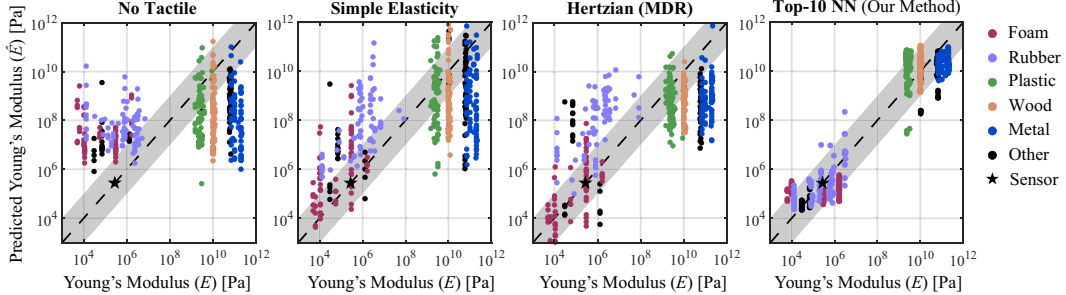


Figure 9: **Young’s modulus predictions by material.** Results for learned and analytical estimation methods are plotted, using predictions from 80 randomly sampled grasps per material category. Predictions in the gray region are considered sufficiently accurate.

accuracy across shape and material categories for each method is investigated in Appendix E. We observe that our model performs independent of shape and can generalize well across materials.

Method	Inputs				Seen Objects		Unseen Objects	
	Depth / RGB	Markers	F	w	$\hat{E}_{\text{elastic}}, \hat{E}_{\text{hertz}}$	Log10 Error	Log10 Acc.	Log10 Error
No Tactile	—	—	✓	✓	—	—	—	2.13 18.2%
	Depth	—	✓	✓	—	—	—	1.90 27.3%
	Depth	—	✓	✓	—	—	—	1.68 28.9%
Top-10 NN (Our Method)	RGB	✓	✓	✓	✓	0.73	76.9%	0.76 73.5%
	RGB	✓	✗	✗	✓	0.73	78.5%	0.76 74.2%
	RGB	✗	✓	✓	✓	0.85	70.4%	0.88 68.6%
	RGB	✗	✗	✗	✓	0.85	69.6%	0.90 67.9%
	RGB	✓	✓	✓	✗	0.63	80.4%	0.86 64.6%
	RGB	✓	✗	✗	✗	0.65	78.5%	0.85 65.0%
	Depth	—	✓	✓	✓	1.05	61.7%	0.98 63.6%
	Depth	—	✗	✗	✓	1.08	60.1%	1.04 59.4%

Table 1: Estimation Architecture Ablation Study

Limitations: Our estimation system struggled to express precise differences in Young’s modulus between harder objects that stray further from the modulus of our sensor (i.e. plastic, wood, and metal objects). These results are expected given that harder objects are rigid relative to our soft sensor. The resolution of our tactile sensor is not high enough to detect minute differences in deformation between this range of compliances. Considering this fact, our estimation system exhibits only marginal effective improvement relative to previously developed Shore hardness estimation models [14]. Further work must be done to create a truly universal compliance estimation system.

7 Conclusion

We have developed a novel system for estimating the Young’s modulus of unknown contacted objects using analytical and data-driven methods. This system can create estimates online from only a single parallel grasp using camera-based tactile sensors. It has been shown to perform independent of object shape and remains robust across material types. It can precisely distinguish between compliances of soft objects, but struggles to expressively differentiate between that of harder objects.

The estimation architecture introduced in this paper could be applied for use with other camera-based tactile sensors capable of tracking depth. With more diverse tactile data, the accuracy of the system could be further improved. Given an increased ability to generalize, this compliance estimation system could be deployed alongside an intelligent high-level controller to inform decision-making in robotic manipulation scenarios by characterizing the compliance of unknown objects. This is particularly valuable when visually similar objects may have distinct material composition. As one example, it could be utilized to identify the ripeness of fruits or vegetables [1, 2, 4].

Acknowledgments

The authors would like to thank Sandra Q. Liu, Jialiang (Alan) Zhao, Megha Tippur, Yuxiang Ma, and Laurence Willemet for their guidance and insight provided throughout the project's duration.

References

- [1] S. Yu, K. Lin, A. Xiao, J. Duan, and H. Soh. Octopi: Object property reasoning with large tactile-language models, 2024.
- [2] L. He, L. Tao, Z. Ma, X. Du, and W. Wan. Cherry tomato firmness detection and prediction using a vision-based tactile sensor. *Journal of Food Measurement and Characterization*, 18(2):1053–1064, Nov. 2023. ISSN 2193-4134. doi:10.1007/s11694-023-02249-0. URL <http://dx.doi.org/10.1007/s11694-023-02249-0>.
- [3] F. E. Erukainure, V. Parque, M. Hassan, and A. M. FathEl-Bab. Estimating the stiffness of kiwifruit based on the fusion of instantaneous tactile sensor data and machine learning schemes. *Computers and Electronics in Agriculture*, 201:107289, 2022. ISSN 0168-1699. doi: <https://doi.org/10.1016/j.compag.2022.107289>. URL <https://www.sciencedirect.com/science/article/pii/S0168169922006019>.
- [4] I. Fahmy, I. Hussain, N. Werghi, T. Hassan, and L. Seneviratne. Hapticformers: Utilizing transformers for avocado maturity grading through vision-based tactile assessment, 02 2024.
- [5] J. Di, Z. Dugonjic, W. Fu, T. Wu, R. Mercado, K. Sawyer, V. R. Most, G. Kammerer, S. Speidel, R. E. Fan, G. Sonn, M. R. Cutkosky, M. Lambeta, and R. Calandra. Using fiber optic bundles to miniaturize vision-based tactile sensors, 2024.
- [6] M. I. Tiwana, S. J. Redmond, and N. H. Lovell. A review of tactile sensing technologies with applications in biomedical engineering. *Sensors and Actuators A: Physical*, 179:17–31, 2012. ISSN 0924-4247. doi:<https://doi.org/10.1016/j.sna.2012.02.051>. URL <https://www.sciencedirect.com/science/article/pii/S0924424712001641>.
- [7] S. Sanan, S. Tully, A. Bajo, N. Simaan, and H. Choset. Simultaneous compliance and registration estimation for robotic surgery. In *Robotics: Science and Systems*, 2014.
- [8] W. M. Bergmann Tiest. Tactual perception of material properties. *Vision Research*, 50(24):2775–2782, 2010. ISSN 0042-6989. doi:<https://doi.org/10.1016/j.visres.2010.10.005>. URL <https://www.sciencedirect.com/science/article/pii/S0042698910004967>. Perception and Action: Part I.
- [9] N. Navarro-Guerrero, S. Toprak, J. Josifovski, and L. Jamone. Visuo-haptic object perception for robots: an overview. *Auton. Robots*, 47(4):377–403, Apr. 2023.
- [10] M. A. Srinivasan and R. H. LaMotte. Tactual discrimination of softness. *J. Neurophysiol.*, 73(1):88–101, Jan. 1995.
- [11] S. Luo, J. Bimbo, R. Dahiya, and H. Liu. Robotic tactile perception of object properties: A review. *Mechatronics*, 48:54–67, 2017. ISSN 0957-4158. doi:<https://doi.org/10.1016/j.mechatronics.2017.11.002>. URL <https://www.sciencedirect.com/science/article/pii/S0957415817301575>.
- [12] W. Yuan, S. Dong, and E. H. Adelson. Gelsight: High-resolution robot tactile sensors for estimating geometry and force. *Sensors*, 17(12):2762, 2017.
- [13] M. R. Cutkosky. *Mechanical properties for the grasp of a robotic hand*. Department of Computer Science, Carnegie-Mellon University, 1984.

[14] W. Yuan, C. Zhu, A. Owens, M. A. Srinivasan, and E. H. Adelson. Shape-independent hardness estimation using deep learning and a gelsight tactile sensor. In *2017 IEEE International Conference on Robotics and Automation (ICRA)*. IEEE, May 2017. doi:10.1109/icra.2017.7989116. URL <http://dx.doi.org/10.1109/ICRA.2017.7989116>.

[15] L. Fu, G. Datta, H. Huang, W. C.-H. Panitch, J. Drake, J. Ortiz, M. Mukadam, M. Lambeta, R. Calandra, and K. Goldberg. A touch, vision, and language dataset for multimodal alignment, 2024.

[16] R. C. Hibbeler. *Mechanics of materials*. MacMillan Publishing Company, 1994.

[17] S. Wang, Y. She, B. Romero, and E. Adelson. Gelsight wedge: Measuring high-resolution 3d contact geometry with a compact robot finger. In *2021 IEEE International Conference on Robotics and Automation (ICRA)*, pages 6468–6475. IEEE, 2021.

[18] I. H. Taylor, S. Dong, and A. Rodriguez. Gelslim 3.0: High-resolution measurement of shape, force and slip in a compact tactile-sensing finger. In *2022 International Conference on Robotics and Automation (ICRA)*, pages 10781–10787. IEEE, 2022.

[19] S. Q. Liu and E. H. Adelson. Gelsight fin ray: Incorporating tactile sensing into a soft compliant robotic gripper, 2022.

[20] M. H. Tippur and E. H. Adelson. Gelsight360: An omnidirectional camera-based tactile sensor for dexterous robotic manipulation, 2023.

[21] J. Zhao and E. H. Adelson. Gelsight svelte hand: A three-finger, two-dof, tactile-rich, low-cost robot hand for dexterous manipulation. *arXiv preprint arXiv:2309.10886*, 2023.

[22] R. Li and E. H. Adelson. Sensing and recognizing surface textures using a gelsight sensor. In *Proceedings of the IEEE Conference on Computer Vision and Pattern Recognition (CVPR)*, June 2013.

[23] S. Luo, W. Yuan, E. Adelson, A. Cohn, and R. Fuentes. Cloth texture recognition using vision and tactile sensing. 05 2018.

[24] A. Amini, J. I. Lipton, and D. Rus. Uncertainty aware texture classification and mapping using soft tactile sensors. In *2020 IEEE/RSJ International Conference on Intelligent Robots and Systems (IROS)*, pages 4249–4256, 2020. doi:10.1109/IROS45743.2020.9341045.

[25] W. Yuan, R. Li, M. A. Srinivasan, and E. H. Adelson. Measurement of shear and slip with a gelsight tactile sensor. In *2015 IEEE International Conference on Robotics and Automation (ICRA)*, pages 304–311, 2015. doi:10.1109/ICRA.2015.7139016.

[26] M. Bauza, O. Canal, and A. Rodriguez. Tactile mapping and localization from high-resolution tactile imprints, 2019.

[27] J. Zhao, M. Bauza, and E. H. Adelson. Fingerslam: Closed-loop unknown object localization and reconstruction from visuo-tactile feedback, 2023.

[28] Z. Si and W. Yuan. Taxim: An example-based simulation model for gelsight tactile sensors, 2021.

[29] D. Ma, E. Donlon, S. Dong, and A. Rodriguez. Dense tactile force estimation using gelslim and inverse fem. In *2019 International Conference on Robotics and Automation (ICRA)*, pages 5418–5424, 2019. doi:10.1109/ICRA.2019.8794113.

[30] I. Taylor, S. Dong, and A. Rodriguez. Gelslim3.0: High-resolution measurement of shape, force and slip in a compact tactile-sensing finger, 2021.

[31] Y. Li and I. Kao. A review of modeling of soft-contact fingers and stiffness control for dexterous manipulation in robotics. In *Proceedings 2001 ICRA. IEEE International Conference on Robotics and Automation (Cat. No.01CH37164)*, volume 3, pages 3055–3060 vol.3, 2001. doi:10.1109/ROBOT.2001.933086.

[32] C. J. Stabile, D. J. Levine, G. M. Iyer, C. Majidi, and K. T. Turner. The role of stiffness in versatile robotic grasping. *IEEE Robotics and Automation Letters*, 7(2):4733–4740, 2022. doi:10.1109/LRA.2022.3149036.

[33] B. W. McInroe, C. L. Chen, K. Y. Goldberg, R. Bajcsy, and R. S. Fearing. Towards a soft fingertip with integrated sensing and actuation. In *2018 IEEE/RSJ International Conference on Intelligent Robots and Systems, IROS 2018, Madrid, Spain, October 1-5, 2018*, pages 6437–6444. IEEE, 2018. doi:10.1109/IROS.2018.8594032. URL <https://doi.org/10.1109/IROS.2018.8594032>.

[34] X. Lin, L. Willemet, A. Bailleul, and M. Wiertlewski. Curvature sensing with a spherical tactile sensor using the color-interference of a marker array. In *2020 IEEE International Conference on Robotics and Automation (ICRA)*, pages 603–609, 2020. doi:10.1109/ICRA40945.2020.9197050.

[35] J. K. Salisbury. Active stiffness control of a manipulator in cartesian coordinates. *1980 19th IEEE Conference on Decision and Control including the Symposium on Adaptive Processes*, pages 95–100, 1980. URL <https://api.semanticscholar.org/CorpusID:1758620>.

[36] K. M. Lynch and F. C. Park. *Modern Robotics: Mechanics, Planning, and Control*. Cambridge University Press, USA, 1st edition, 2017. ISBN 1107156300.

[37] C. Ciliberto, L. Fiorio, M. Maggiali, L. Natale, L. Rosasco, G. Metta, G. Sandini, and F. Nori. Exploiting global force torque measurements for local compliance estimation in tactile arrays. In *2014 IEEE/RSJ International Conference on Intelligent Robots and Systems*, pages 3994–3999, 2014. doi:10.1109/IROS.2014.6943124.

[38] G. Kinoshita, Y. Sugeno, H. Oosumi, K. Umeda, and Y. Muranaka. High compliance sensing behavior of a tactile sensor. In *Proceedings 1999 IEEE/RSJ International Conference on Intelligent Robots and Systems. Human and Environment Friendly Robots with High Intelligence and Emotional Quotients (Cat. No.99CH36289)*, volume 2, pages 826–831 vol.2, 1999. doi:10.1109/IROS.1999.812782.

[39] Z. Su, J. Fishel, T. Yamamoto, and G. Loeb. Use of tactile feedback to control exploratory movements to characterize object compliance. *Frontiers in neurorobotics*, 6:7, 07 2012. doi:10.3389/fnbot.2012.00007.

[40] W. Yuan, M. A. Srinivasan, and E. H. Adelson. Estimating object hardness with a gelsight touch sensor. In *2016 IEEE/RSJ International Conference on Intelligent Robots and Systems (IROS)*, pages 208–215, 2016. doi:10.1109/IROS.2016.7759057.

[41] A. N. Gent. On the relation between indentation hardness and young's modulus. *Rubber Chemistry and Technology*, 31:896–906, 1958. URL <https://api.semanticscholar.org/CorpusID:136730823>.

[42] A. Zeng, S. Song, J. Lee, A. Rodriguez, and T. Funkhouser. Tossingbot: Learning to throw arbitrary objects with residual physics. 2019.

[43] H.-J. Huang, X. Guo, and W. Yuan. Understanding dynamic tactile sensing for liquid property estimation, 2022.

[44] J. Mahler, J. Liang, S. Niyaz, M. Laskey, R. Doan, X. Liu, J. A. Ojea, and K. Goldberg. Dexnet 2.0: Deep learning to plan robust grasps with synthetic point clouds and analytic grasp metrics, 2017.

- [45] H. Hertz. The contact of elastic solids. *J Reine Angew. Math*, 92:156–171, 1881.
- [46] V. L. Popov et al. *Contact mechanics and friction*. Springer, 2010.
- [47] K. L. Johnson. *Contact mechanics*. Cambridge university press, 1987.
- [48] V. L. Popov, M. Heß, and E. Willert. *Handbook of contact mechanics: exact solutions of axisymmetric contact problems*. Springer Nature, 2019.
- [49] W. Zunker and K. Kamrin. A mechanically-derived contact model for adhesive elastic–perfectly plastic particles. part i: Utilizing the method of dimensionality reduction, 2023.
- [50] G. N. Greaves, A. L. Greer, R. S. Lakes, and T. Rouxel. Poisson’s ratio and modern materials. *Nat. Mater.*, 10(11):823–837, Oct. 2011.
- [51] B. Calli, A. Singh, J. Bruce, A. Walsman, K. Konolige, S. Srinivasa, P. Abbeel, and A. M. Dollar. Yale-CMU-Berkeley dataset for robotic manipulation research. *Int. J. Rob. Res.*, 36(3):261–268, Mar. 2017.
- [52] Material property data. *MatWeb*, 2024. URL <https://www.matweb.com/>.
- [53] K. Larson. Can you estimate modulus from durometer hardness for silicones? yes, but only roughly . . . and you must choose your modulus carefully! *Dow White Paper*, 09 2017.
- [54] E. Finney. Dynamic elastic properties of some fruits during growth and development. *Journal of Agricultural Engineering Research*, 12(4):249–256, 1967. ISSN 0021-8634. doi:[https://doi.org/10.1016/S0021-8634\(67\)80043-X](https://doi.org/10.1016/S0021-8634(67)80043-X). URL <https://www.sciencedirect.com/science/article/pii/S002186346780043X>.
- [55] L. Fariñas, E. A. Sanchez-Torres, V. Sanchez-Jimenez, R. Diaz, J. Benedito, and J. V. Garcia-Perez. Assessment of avocado textural changes during ripening by using contactless air-coupled ultrasound. *Journal of Food Engineering*, 289:110266, 2021. ISSN 0260-8774. doi: <https://doi.org/10.1016/j.jfoodeng.2020.110266>. URL <https://www.sciencedirect.com/science/article/pii/S0260877420303563>.
- [56] M. Ibrahim and A. Hassan. Elastic properties of three varieties of date fruits during three different ripening stages. *Misr Journal of Agricultural Engineering*, 29:1125 – 1148., 01 2012. doi:[10.21608/mjae.2020.101822](https://doi.org/10.21608/mjae.2020.101822).
- [57] F. Babarinsa and M. Ige. Young’s modulus for packaged roma tomatoes under compressive loading. 3, 01 2012.
- [58] V. Popov and M. Heß. Method of dimensionality reduction in contact mechanics and friction: A users handbook. i. axially-symmetric contacts. *Acta Universitas*, 12:1–14, 04 2014.

A Method of Dimensionality Reduction (MDR)

As discussed in Section 3.2, we model contact between an unknown object and our flat, camera-based tactile sensor as a collision between an elastic sphere and an elastic half-space using Hertzian contact theory. Now, we will walk through the derivation for a constitutive relation using the method of dimensionality reduction (MDR) [58]. A mechanical diagram of contact at time t with labeled variables is provided in Fig. 10.

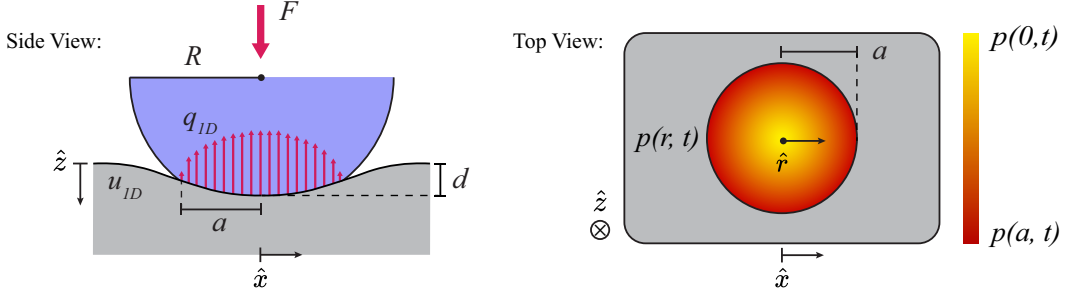


Figure 10: **Method of dimensionality reduction (MDR) diagram.** An elastic sphere is colliding with an elastic half-space at time t . Variables of contact are labeled. The two-dimensional radial stress field p is transformed into a one-dimensional force field q_{1D} . This transformation can be observed through comparison of top and side views.

First, we compute the maximum pressure of contact p_0 between both bodies in Eq. 6. This is a simple expression of measured force F and contact radius a . We can substitute a to create an expression dependent on the aggregate elastic compliance of the bodies E^* [47].

$$p_0(t) = \frac{3F(t)}{2\pi a^2(t)} = \frac{1}{\pi} \left(\frac{F(t)E^{*2}}{R^2} \right)^{\frac{1}{3}} \quad (6)$$

Using this maximum pressure p_0 at timestep t , we create the radial pressure field of contact $p(r, t)$. This expression comes directly from Hertzian contact theory [47].

$$p(r, t) = p_0(t) \sqrt{1 - \frac{r^2}{a^2(t)}} \quad (7)$$

Now, we will apply the method of dimensionality reduction (MDR). This technique is used to solve the stress field for surface deformation based on the assumption that contact geometries are axisymmetric. By utilizing this method, we are able to reconstruct the deformation of the sensor surface. We begin by transforming coordinates of the pressure field into one-dimensional force density q_{1D} through Eq. 8.

$$q_{1D}(x, t) = 2 \int_x^\infty \frac{rp(r, t)}{\sqrt{r^2 - x^2}} dr \quad (8)$$

From here, we apply a constitutive relationship on the sensor gel pad to get a one-dimensional displacement of the gel surface u_{1D} . This displacement is defined in the normal direction \hat{z} . By transforming to a single dimension, we restrict the displacement geometry to be axisymmetric about \hat{z} from the center $x = 0$.

$$u_{1D}(x, t) = \left(\frac{1 - \nu_{\text{sensor}}^2}{E_{\text{sensor}}} \right) q_{1D}(x, t) \quad (9)$$

The maximum displacement will occur at $x = 0$. We define this to be equivalent to our maximum measured depth d .

$$u_{1D}(0, t) = d(t) = \left(\frac{1 - \nu_{\text{sensor}}^2}{E_{\text{sensor}}} \right) q_{1D}(0, t) \quad (10)$$

Then, by plugging in $x = 0$, the expression for q_{1D} simplifies considerably.

$$u_{1D}(0, t) = d(t) = 2 \left(\frac{1 - \nu_{\text{sensor}}^2}{E_{\text{sensor}}} \right) \int_0^{a(t)} p(r, t) dr \quad (11)$$

We solve this integral to get Eq. 13 which expresses maximum observed surface displacement d in terms of normal force F .

$$\int_0^{a(t)} p_0(t) \sqrt{1 - \frac{r^2}{a^2(t)}} dr = \frac{\pi}{4} p_0(t) a(t) = \left(\frac{3F(t)E^{*2}}{32R^2} \right)^{\frac{1}{3}} a(t) \quad (12)$$

$$u_{1D}(0, t) = d(t) = \frac{1 - \nu_{\text{sensor}}^2}{E_{\text{sensor}}} \left(\frac{3E^{*2}F(t)}{32R^2(t)} \right)^{\frac{1}{3}} a(t) \quad (13)$$

We apply this relation for every timestep t over the duration of a grasp. Using all measurements of d , a , and F , we can apply a linear least-squares algorithm to retrieve a best fit value \hat{E}^* . Then, this estimate is used with known mechanical properties of our sensor's silicone gel pads to compute the Young's modulus of the unknown grasped object \hat{E}_{hertz} , as shown in Eq. 5.

Without the MDR, we could not have solved directly for the deformation of the gel surface, meaning we could not create an expression relating F directly to d in terms of Young's modulus. Instead, we could only derive a relation for the apparent deformation of both bodies with respect to each other. This apparent deformation is equal to the displacement between both bodies, or change in gripper width Δw in our case. This is a classic tabulated solution for Hertzian contact between a sphere and a plane [47], written as Eq. 14.

$$F(t) = 2E^*a(t)\Delta w(t) \quad (14)$$

Notably, this model would not make use of tactile depth d and relies solely on gripper width w measurements. These gripper measurements exhibit a larger observed error than tactile depth measurements, which are higher-resolution and demonstrate sub-millimeter accuracy. For these reasons, we opt to use the MDR-derived solution.

B Markers

Markers are small black dots painted in an array on the surface of the GelSight gel pad. As the surface of the gel deforms and stretches, these markers move. Thus, we can track their relative position to map the displacement of the gel pad surface in both shear and normal directions. Markers have been shown to be effective in estimating shear and normal forces from tactile images [12, 17]. However, accurate force estimations require assumptions on contact geometry. In this work, we seek to estimate the compliance of unknown objects. Since we cannot make accurate assumptions on geometry, we measure forces through an external force gauge rather than through our GelSight sensors. In any case, we can use markers to increase the amount of dynamic information encoded in a tactile image. Without them, we could not perceive shear displacement.

In our experiment, we have created one GelSight Wedge [17] with markers painted on the surface. This was done to investigate how beneficial markers may be for estimating a dynamic property of contact like Young's modulus. The difference between tactile images with or without markers for two objects is displayed in Fig. 11. These markers help track surface displacement, but they may occlude fine features of texture, like screw threads.

C Processing Grasp Data

We collect data over a set number of automated parallel grasps for every object in our dataset. Normal force F , width w , and maximum depth d are plotted for an example grasp of a rigid sphere in Fig. 12a. Grasps are executed at nearly constant velocity to a peak force of approximately 30 N.

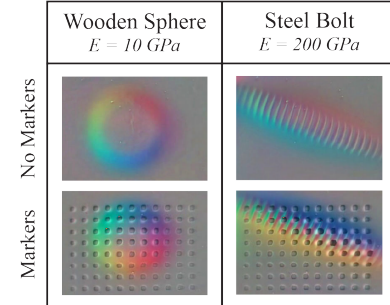


Figure 11: **Markers.** Tactile images from GelSight Wedge's with and without markers. Tactile images are size 35mm by 25mm.

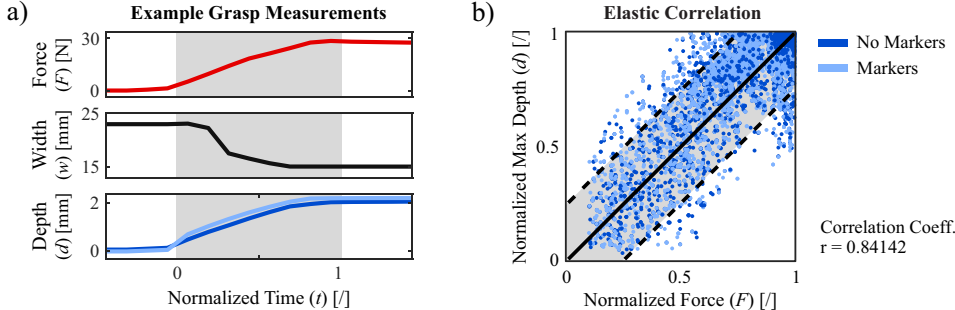


Figure 12: **Grasping data.** (a) Grasp data is plotted for an example grasp of a rigid sphere. The chosen loading sequence from initial contact to peak force is highlighted in gray. (b) Normalized force and depth measurements from all collected grasps are plotted. The correlation coefficient between these measurements is computed as 0.84 and bounds are placed at 25% error mark.

These measurements are clipped to the loading sequence based on force thresholding. Once force passes an empirically-defined threshold of 0.75 N, we consider the object to be in-contact with the GelSight sensor and define this as timestep $t = 0$. We clip data from this point until the peak recorded force is reached.

As expected in an elastic regime, we observe that force and depth measurements are high correlated from both GelSight sensors. Raw collected data normalized per grasp is plotted in Fig. 12b. Measurements are normalized according to their peak value over each respective grasp. These measurements are randomly sampled from grasps across the entire dataset. All measurements outside of 25% correlation bounds are discarded. Over 90% of measured points lie within these bounds for both sensors. We observe that there is no distinguishable difference between measurements collected from one sensor to the other.

D Comparison Against Shore 00 Hardness Baseline

Previous works have developed learning-based methods to estimate Shore hardness using camera-based tactile sensors without the incorporation of analytical modelling [40, 14, 5, 15, 1]. Notably, Yuan et al. introduced an architecture to estimate Shore 00 hardness of various sample geometries using tactile images captured from a GelSight sensor [14]. To demonstrate the performance of our novel hybrid estimation system, we directly compare it against results from Yuan et al.

As discussed in Section 6, we can constrain our dataset to predict compliance for only rubber objects. There are 82 rubber objects in our dataset of 285 total objects. The compliance of these rubber objects aligns with the Shore 00 hardness scale, which spans approximately from a Young’s modulus of 6 kPa to 2 MPa. We can directly evaluate and compare predictions of Young’s modulus with Shore 00 hardness by utilizing established models that convert between the two measures [53].

Using the rubber subset of our dataset, we replicate experiments conducted by Yuan et al. and compare their quoted results against our own [14]. We use RGB tactile images with markers and analytical estimates as the input to our model. First, we train an instance of our hybrid estimation system to predict compliance using only simple shapes such as spheres, cylinders, and rectangular objects. This model is validated across seen shapes with unseen compliances. Predictions from our model are subsequently converted to Shore 00 hardness to calculate error over the validation set. Second, we train another instance of our hybrid model and validate it across unseen objects with arbitrary or irregular shapes. It is important to note that Yuan et al. evaluate over hand-collected data for the latter experiment, whereas all of our data collection is performed on robot hardware. Results from our experiments are presented in Table 2, where root mean-squared error (RMSE) is reported in units of Shore 00 hardness.

Our estimation system exhibits decreased error in both experiments across both simple and complex shapes, though the margin of improvement is modest. These results suggest that our novel hybrid

Method	Dataset	R^2	RMSE
Shore 00 Hardness Model [14]	Simple Shapes	0.85	10.3
	Arbitrary Shapes	0.39	18.2
Top-1 Hybrid NN (Our Method)	Simple Shapes	0.69	5.9
	Arbitrary Shapes	0.37	14.3

Table 2: Shore 00 Hardness Prediction Error Comparison

estimation architecture offers some performance enhancement over previously developed learning-based approaches for predicting the compliance of soft rubbers. We can likely attribute this decrease in error to the incorporation of analytical modeling.

E Dataset Diversity & Performance

The diversity of the collected dataset is characterized through categories of material and shape in Tables 3 and 4. As intended, the most common material of objects in the dataset is rubber, which includes 28.6% of the objects in the dataset. This is done to bias the dataset toward the Young's modulus of our sensor's gel pads. There are significant percentages of metal and plastic objects, making up 25.1% and 24.0% of the dataset respectively. Over 50% of objects in the dataset have irregular shapes. This is done to diversify training data in an attempt and learn Young's modulus independent of object shape or contact profile. Still, there are substantial percentages of simple shapes for performance evaluation.

Table 3: Dataset Material Distributions

Material	Percent (%)
Rubber	28.6%
Metal	25.1%
Plastic	24.0%
Wood	8.4%
Foam	6.3%
Other	7.6%

Table 4: Dataset Shape Distributions

Shape	Percent (%)
Cylinder	20.2%
Sphere	11.5%
Rectangular	15.3%
Hexagonal	2.1%
Irregular	50.9%

Results of investigated methods on unseen objects across shape and material categories are compared in Fig. 13. We observe that neural network methods give the lowest log10 error and accuracy in nearly every category. Moreover, the accuracy increases and error decreases with the complexity of analytical models. Our Hertzian method performs best over spheres, which is expected given that this model assumes spherical contact geometry. Most critically, it is shown that our trained model can learn Young's modulus independent of shape, given that prediction accuracy and error remain consistent across different object shapes. The model performs robustly across different categories of materials as well.

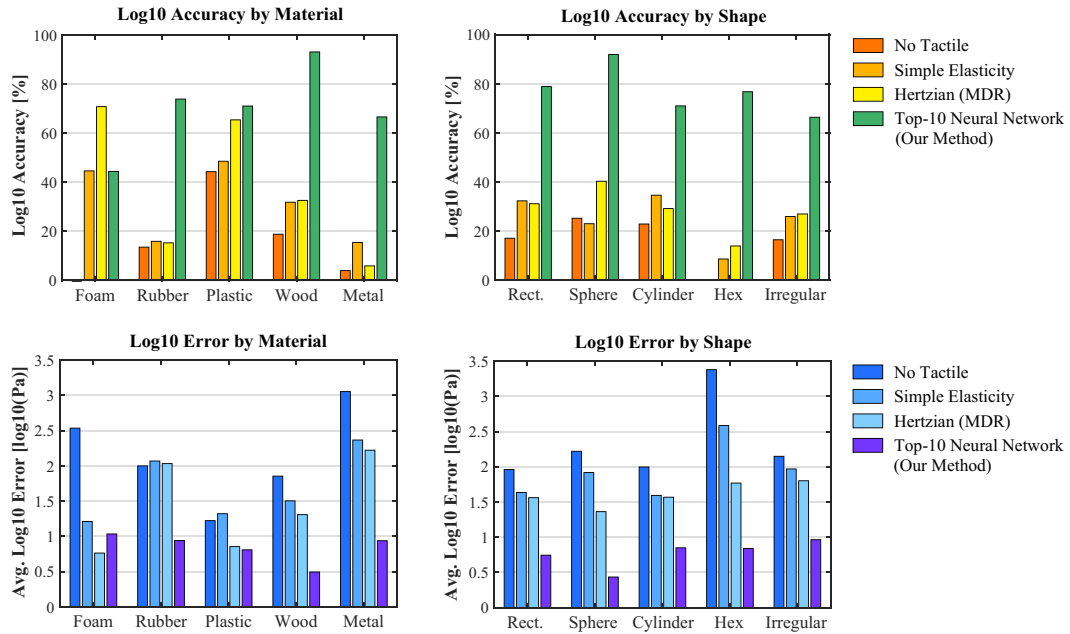


Figure 13: **Estimation methods performance.** Log10 error and accuracy are plotted for each estimation method across dataset categories of shape and material. Neural network results are from top-10 trained models evaluated on unseen objects.